OPEN ACCESS
IOP Publishing | Songshan Lake Materials Laboratory
Materials Futures
Mater. Futures 1 (2022) 022001 (17pp)
https://doi.org/10.1088/2752-5724/ac52e8

Topical Review

Unleashing energy storage ability of aqueous battery electrolytes

Hongmei Tang[1,2], Zhe Qu[1,2], Yaping Yan[1,2], Wenlan Zhang[1,2], Hua Zhang[3], Minshen Zhu[1,*] and Oliver G Schmidt[1,2,4]

[1] Center for Materials, Architectures, and Integration of Nanomembranes (MAIN), TU Chemnitz, 09126 Chemnitz, Germany
[2] Material Systems for Nanoelectronics, TU Chemnitz, 09107 Chemnitz, Germany
[3] Sustainable Materials and Chemistry, Department of Wood Technology and Wood-based Composites, University of Goettingen, 37077 Göttingen, Germany
[4] School of Science, TU Dresden, 01062 Dresden, Germany

E-mail: minshen.zhu@main.tu-chemnitz.de

Received 3 January 2022, revised 3 February 2022
Accepted for publication 8 February 2022
Published 14 April 2022

Abstract

Electrolytes make up a large portion of the volume of energy storage devices, but they often do not contribute to energy storage. The ability of using electrolytes to store charge would promise a significant increase in energy density to meet the needs of evolving electronic devices. Redox-flow batteries use electrolytes to store energy and show high energy densities, but the same design cannot be applied to portable or microdevices that require static electrolytes. Therefore, implementing electrolyte energy storage in a non-flow design becomes critical. This review summarizes the requirements for a stable and efficient electrolyte and diverse redox-active species dissolved in aqueous solutions. More importantly, we review the pioneering works using static electrolyte energy storage in the hope that it will pave a new way to design compact and energy-dense batteries.

Keywords: aqueous batteries, redox-active electrolytes, redox-flow batteries, cathode-less, anode-less

(Some figures may appear in colour only in the online journal)

1. Introduction

Electrochemical energy storage (EES) devices sit at the heart of the de-fossilization strategy towards carbon neutrality because it is essential to store energy from intermittent renewable sources (e.g. solar and wind) [1–3]. Among various EES devices, supercapacitors are able to operate at a high specific power (>10 kW kg^{-1}), delivering the stored energy within tens of seconds and lasting for over 10^5 charge/discharge cycles [4]. Their charge storage mechanisms, electrical double-layer (EDL) formation and surface redox reactions, enable these particular properties of supercapacitors [5]. The EDL is formed (type-i in figure 1(A)) upon the physical adsorption of charged ions in the electrolyte on the electrode surface. The reversible sorption of dissolved ions in the electrolyte is a fast and non-Faradaic process, avoiding any significant structural variation and allowing for high-power capability and cycling stability. Porous carbonaceous materials are widely used as electrodes in electrical double-layer capacitors (EDLCs) owing to their large surface area providing plenty of adsorption sites [6]. In addition to EDLCs, pseudocapacitive electrode

* Author to whom any correspondence should be addressed.

Future perspectives
Electrode materials that store and release charges are the focus of developing energy storage systems. The electrolyte usually has to be adapted to the design of the electrode material. Alternatively, redox-flow batteries, a successful design for large-scale energy storage requiring high energy and safety, utilize electrolytes to store energy, which reveals the potential of unleashing the charge storage ability of electrolytes. Recent encouraging developments on anode-free or cathode-free are broadly in line with this design principle. If the same mechanism can be implemented in portable or even microscale devices, it will also provide more possibilities for the design of next-generation electronic devices.

materials store charge via Faradaic processes based on fast and reversible redox reactions at the surface or near-surface positions (type-ii in figure 1(A)). The main disadvantage of supercapacitors is their limited energy density (<10 Wh kg^{-1}). By contrast, batteries show a much-improved energy density of ∼300 Wh kg^{-1} [4, 7]. The trade-offs of the high energy density are short cycle life, a few thousand cycles for instance, and lower power density. Such differences against supercapacitors originate from the slow charge storage mechanism based on bulk redox reactions relying on the solid-state diffusion of ions. The structural changes of the bulk electrode materials build up and eventually cause battery failure. The intercalation pseudocapacitor is a promising design to combine the advantage of supercapacitors and batteries. Like lithium-ion batteries, ions dissolved in the electrolyte (e.g. Li^+, Na^+, K^+, and H^+) and also intercalate into the bulk electrode materials (type-iii in figure 1(A)) but with fast kinetics [8, 9].

The electrolyte in the above EES devices only acts as a medium to transfer and balance charges between electrodes and therefore does not contribute to energy storage. As such, the thinner the electrolyte layer is, the higher energy density can be achieved for EES devices. Alternatively, redox-active species dissolved in the electrolyte can substitute the function of electrode materials to store charges by redox reactions at the solid-liquid interface (figure 1(B)). Redox flow designs are an excellent approach to demonstrate the charge storage in the electrolyte. For instance, vanadium (V) and oxidized vanadium ions are used in the redox flow battery. Upon charging, VO^{2+} ions are oxidized to $VO_2{}^+$, and V^{3+} is reduced to form V^{2+}. Inversely, $VO_2{}^+$ is reduced to VO^{2+}, and V^{2+} is oxidized to V^{3+} during discharge (figure 1(C)) [10]. The redox flow batteries usually need electrolyte tanks to refill and circulate electrolytes. The same strategy is adopted at small scale in cathode-less (figure 1(D)) and anode-less (figure 1(F)) designs. For instance, MnO_2 solids are deposited on the current collector by oxidizing soluble Mn^{2+} ions in the electrolyte (figure 1(E)). The reversible reaction between Mn^{2+} and MnO_2 allows for the design of a secondary battery. The same principle applies to the *in-situ* formation of anode materials. Zn can be deposited on a conductive substrate under a negative potential (figure 1(G)).

By unleashing the energy storage ability of electrolytes, it is possible to substantially improve the energy density of batteries and open a new world for developing energy-dense and small-scale batteries. This article reviews the electrochemical basics of redox-active electrolytes and introduces representative redox-active species for diverse battery designs. Last but not least, we highlight the pioneering works on the concept of storing energy in the electrolyte and discuss the perspectives of batteries based on redox-active electrolytes.

2. Redox-active electrolytes for batteries

2.1. Basic parameters for a redox-active electrolyte

Electrolytes need to exhibit high ionic conductivity, wide electrochemical windows, and high chemical and thermal stability. For redox-active electrolytes, a large potential difference between redox couples and multiple electron transfer of redox reactions are required to reach a high energy density [11]. At the device level, a high concentration of redox couples can improve the energy storage ability of the full cell. In practice, the electrochemical window, redox couples, and kinetics in mass and electron transport are three basic parameters.

The electrochemical stability window of water is ∼1.23 V at 25 °C, above which oxygen evolution reaction (OER) on the positive electrode and hydrogen evolution reaction (HER) on the negative electrode will occur. However, the actual water decomposition process usually requires an overpotential (η) to overcome the intrinsic activation barriers of HER and OER and resistance in the system (e.g. solution and interface resistance). Thus, the practical stability of aqueous solutions is often slightly higher than 1.23 V [12]. Figure 2(A) shows the potentials of OER and HER varies as a function of pH value, where OER potential shifts to a higher potential in acid (59 mV/pH) and HER potential shifts to a lower potential in alkaline (−59 mV/pH). Thus, the pH-decoupling strategy, which separates the acidic electrolyte at the positive side (referred to as catholyte) and alkaline electrolyte at the negative side (referred to as anolyte) by an ion-selective membrane, provides a wide voltage range of ∼3 V [13].

The potential difference between redox couples determines the operation voltage of the cell (figure 2(B)) [14]. As illustrated in figure 1(C), oxidized vanadium species and vanadium cations are separated by an ion-selective membrane, and the redox reactions are independent of each other. The overall voltage (1.26 V) is determined by redox potentials of $VO_2{}^+/VO^{2+}$ (+1.00 V vs standard hydrogen electrode (SHE)) and V^{3+}/V^{2+} (−0.26 V vs SHE) [15]. Besides, a mixture electrolyte would also be possible for specific redox reactions at different electrodes. For example, redox reactions for Zn^{2+} and Br^- ions are able to individually occur at the anode and cathode in $ZnBr_2$ solution (figure 1(G)) [16].

The redox potential of redox couples is also influenced by the concentration of the electrolyte following the Nernst equation:

$$E = E^{0'} + \frac{RT}{nF}\ln\frac{[\mathrm{Ox}]}{[\mathrm{Re}]}$$

where E is the potential of the half-cell with a redox couple of oxidized (Ox) and reduced (Re) analyte, R is the universal gas constant (8.31 J K^{-1} mol^{-1}), T is the temperature in Kelvin, n is the number of the transferred electrons, F is the Faraday's

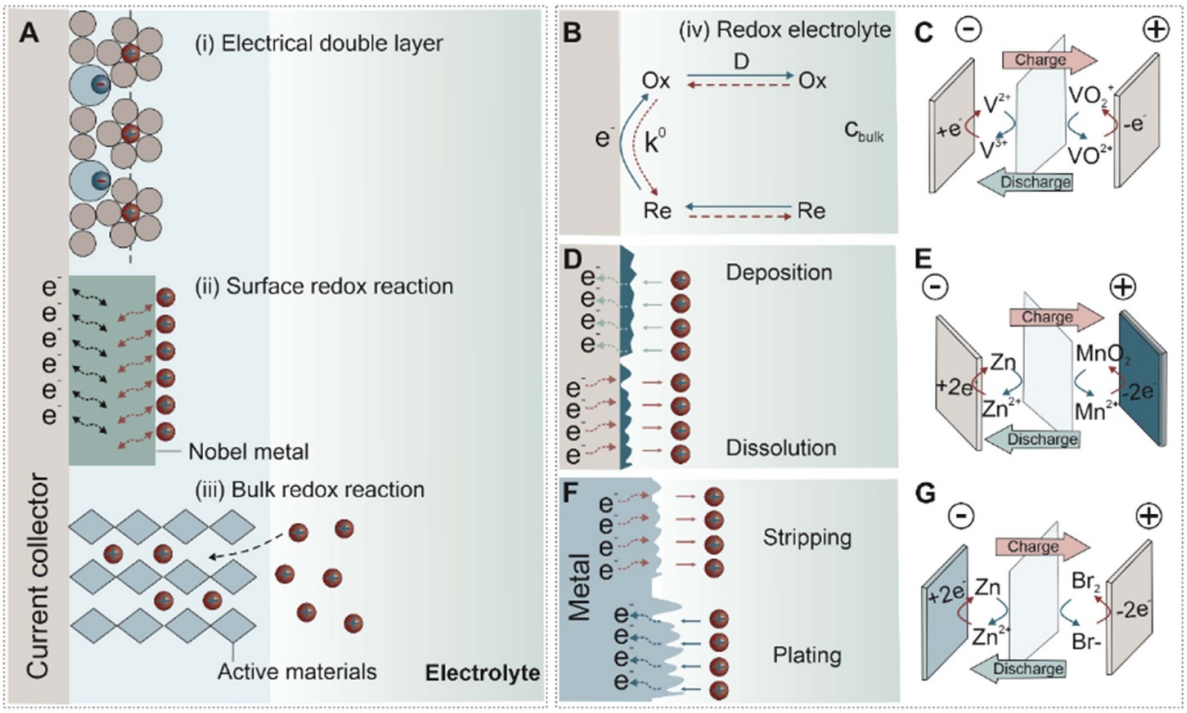

Figure 1. Charge storage mechanisms for EES. (A) Schematic illustration of EDL formation, surface redox reaction, and bulk redox reaction. Reproduced with permission [5]. Copyright 2019, Elsevier. CC BY 4.0. Redox reactions of soluble active species (B), deposition/dissolution process (D), and stripping/plating of metal (F). (C), (E), and (G) Examples of the redox reactions in rechargeable batteries. Reproduced with permission [10] Copyright 2012, Royal Society of Chemistry. Ox and Re represent the oxidation and reduction products, respectively. C_{bulk} is the concentration of Ox and Re in the bulk electrolyte. D represents diffusion coefficient and k^0 is the kinetic rate constant.

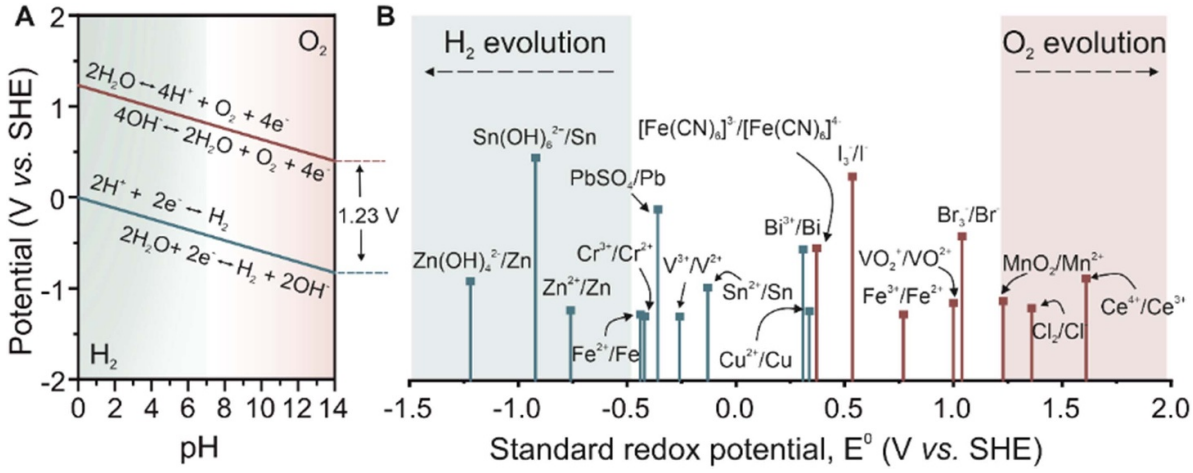

Figure 2. Electrochemically stable potential window and redox potentials of redox-active couples. (A) Pourbaix diagram of water. Reproduced with permission [13]. Copyright 2020, Elsevier. (B) Standard redox potential of reversible inorganic redox couples. Highlighting regions are HER (green) and OER (pink). Reproduced with permission [14]. Copyright 2011, American Chemical Society.

constant (96 485.33 C mol^{-1}), and [Ox] and [Re] are the concentrations of the active species at the electrode surface. $E^{0'}$ is the formal potential defined by the following equation:

$$E^{0'} = E^0 + \frac{RT}{nF}\ln\frac{\gamma_{\text{Ox}}}{\gamma_{\text{Re}}}$$

where E^0 is the standard redox potential of the Ox/Re couple, γ_{Ox} and γ_{Re} are activity coefficients of oxidized and reduced species, respectively. The formal potential shifts with the variation of ionic strength of the electrolyte. For instance, the standard potential of the $Fe(CN)_6^{3-}/Fe(CN)_6^{4-}$ redox couple is 0.36 V (vs SHE), while the formal potential can reach around 0.44 V (vs SHE) in a solution with an ionic strength equivalent to a 0.5 M salt solution [17]. Additionally, pH values determine the potentials of water electrolysis that relate to the electrochemical window of electrolytes and

redox reactions involving protons. The redox potential for redox couple based on m mol H^+ with n mol e^- exchange will change at a rate of $-\frac{m}{n} \times 59$ mV/pH at 25 °C [18]. Meanwhile, pH also plays an important role in the stability of redox couples [19].

Electrochemical reactions are heterogeneous with two successive processes: (a) the mass transport for the active species across the diffusion layer and (b) the kinetics for charge transfer across the electrolyte-electrode interface. Fast mass transport and electron-transfer kinetics allow for high energy efficiency and power density. The diffusion coefficient (D) is usually evaluated by a hydrodynamical method that records linear sweep voltammetry (LSV) curve with a rotating disc electrode (RDE) [20]. The D value can be determined through the Levich equation:

$$i_{\text{lim}} = 0.62nFAD^{\frac{2}{3}}\omega^{\frac{1}{2}}\upsilon^{\frac{-1}{6}}c$$

where A is the geometric area of the working electrode in cm^2, ω is the angular velocity of the RDE in rad s^{-1}, υ is the kinematic viscosity of the electrolyte in cm^2 s^{-1}, and c is the concentration of active species in mol cm^{-3}. As the reaction kinetics also influence the current in actual cells, a better expression for quasi-reversible reactions is given, which is known as Koutecký-Levich equation:

$$\frac{1}{j} = \frac{1}{j_k} + \frac{1}{0.62nFAD^{\frac{2}{3}}\omega^{\frac{1}{2}}\upsilon^{\frac{-1}{6}}c}$$

where j is the current density, and j_k represents the current density in the absence of any mass-transfer effects. The determination of j_k at different values of E derives the kinetic rate constant (k^0). The standard rate constant (k^0) represents the kinetics of a redox couple. A large k^0 value indicates the Nernstian equilibrium can be established immediately due to the low barrier of electron transfer. On the contrary, a small k^0 value implies the sluggish kinetics associated with a high barrier to electron transfer.

The results of peak currents obtained from a series of cyclic voltammetry (CV) measurements at various scan rates are brought into the Randles-Sevcik equation to derive the D value. In specific, the peak current shows a linear increase with the square root of the scan rate for a reversible system. The obtained slope is proportional to the D value. Nevertheless, the accuracy of the result may be impacted by capacitive effects [21]. Chronoamperometry measurements can yield the D value in a single experiment through the Cottrell equation [22–24]. An important parameter applied in the equation is the area of an electrode. The difference between the geometric area and the electrochemically active area would influence the results. By contrast, the definition of D value by LSV has a high accuracy due to the minimization of capacitive effects and natural conditions. On the other hand, the k^0 value also can be yielded by the Nicolson method based on a series of CV measurements which are the same as the CV techniques carried out for deriving the D value [25]. Both D and k^0 are essential parameters in any electrochemical process and have been discussed in detail in another focused review [26].

2.2. Water-soluble inorganic redox couples

2.2.1. All-soluble redox couples

2.2.1.1. Vanadium-based redox couples. Vanadium (V) is an element with multiple valence states, among which V (+2, +3, +4 and +5) are typical redox-active species applied in redox flow batteries. The corresponding ions are V^{2+}, V^{3+}, VO^{2+} and VO_2^+ in sulfate solution. Redox reactions are:

$$V^{3+} + e^- \leftrightarrow V^{2+} \quad E^0 = -0.26 \text{ V vs SHE}$$

$$VO^{2+} + 2H^+ + e^- \leftrightarrow V^{3+} + H_2O \quad E^0 = 0.34 \text{ V vs SHE}$$

$$VO_2^+ + 2H^+ + e^- \leftrightarrow VO^{2+} + H_2O \quad E^0 = 1.00 \text{ V vs SHE.}$$

All redox-active cations can be generated reversely in a mixed electrolyte, circumventing the cross-contamination issue of decoupled electrolyte designs. The V^{3+}/V^{2+} couple shows a negative standard redox potential of −0.26 V, thus acting as an anolyte. For the catholyte, the VO_2^+/VO^{2+} couple is employed due to its 1 V redox potential. The full-cell voltage reaches more than 1 V. The redox potential of VO_2^+/VO^{2+} changes at a rate of −59 mV per pH, while the potential of the V^{3+}/V^{2+} redox reaction is pH-independent [27].

The solubility of $VOSO_4$ (V^{4+} compound) and the stability of V^{5+} cations impose a limit on the working temperature range of −5 °C∼40 °C. More specific, 2 M VO_2^+ dissolved in 5 M H_2SO_4 precipitates at −5 °C after only 18 h, and V_2O_5 precipitation is observed at above 40 °C through the hydrolysis reaction of VO_2^+:

$$2VO_2^+ + H_2O \leftrightarrow V_2O_5 + 2H^+.$$

The stability of VO_2^+ cations increases at a higher concentration of sulfuric acid because excessive protons change the reaction quotient. A high concentration of H_2SO_4 increases the viscosity and therefore limits the mass transportation of active species. The employment of a mixed sulfate-chloride electrolyte is able to increase the solubility and enhance the stability of VO_2^+ in a wide range of operating temperatures [28, 29]. As a result, this system yields an approximately 70% increase in energy densities compared to the sulfuric-acid-based system. Li *et al* [29] reported a sulfate-chloride mixed solution (2.5 M H_2SO_4 and 6 M HCl) capable of dissolving 2.5 M vanadium cations. This battery has a wide temperature range of −5 °C to 50 °C. Such a temperature range expansion is attributed to the formation of stable $VO_2Cl(H_2O)_2$ at elevated temperatures (>20 °C) (figure 3(A)). Moreover, the electron transfer kinetics was improved, as evidenced by an increased peak current in CV curves of vanadium redox reaction in the sulfate-chloride mixed solution (figure 3(B)). Agarwal *et al* [30] elaborated that the charge transfer through the chloride bridge in HCl possesses higher polarizability than through surface-bound hydroxyl groups in H_2SO_4 and HCl/H_2SO_4, resulting in faster V^{3+}/V^{2+} kinetics. However, HCl vapor at a high temperature and Cl_2 evolution due to overcharging

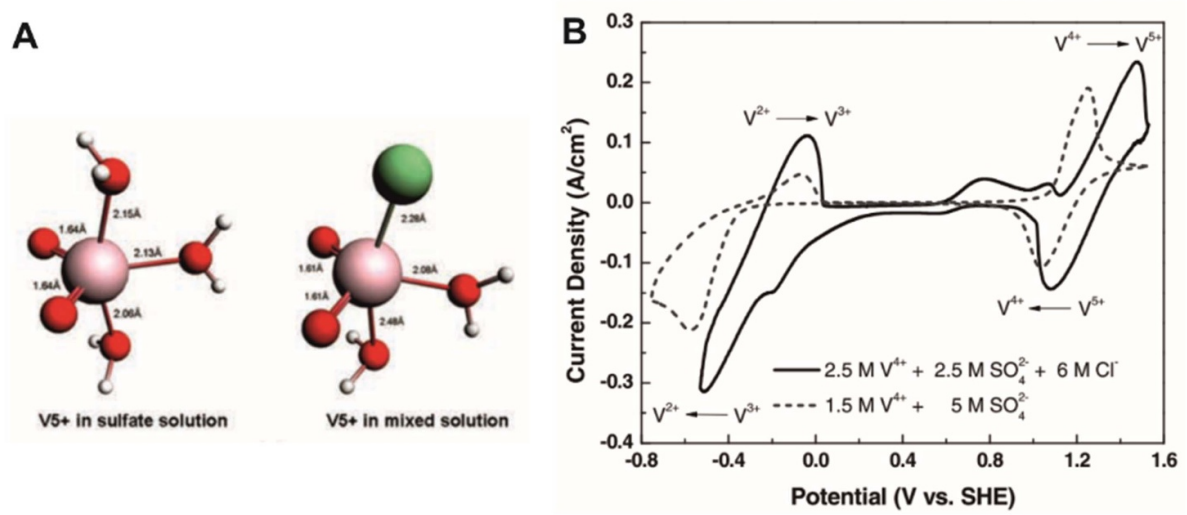

Figure 3. Vanadium-based redox couples in sulfate and sulfate-chloride mixed electrolyte. (A) The structures of V^{5+} complexes in the sulfate and the mixed electrolyte. The VO_2^+ ions form a bipyramidal $[VO_2(H_2O)_3]^+$ structure in sulfate solution and a stable $VO_2Cl(H_2O)_2$ structure in the mixed electrolyte. (B) CV curves of vanadium flow battery on graphite felt electrode in a standard sulfate electrolyte and the mixed electrolyte, respectively. Reproduced with permission [29]. Copyright 2011, John Wiley & Sons.

reduces the advantage of the fast reaction kinetics. Alternatively, catalysts, such as Bi [31, 32], Pt [33], and Ir [34], Mn_3O_4 [35, 36], MoO_2 [37], GeO_2 [38], and WO_3 [39], and surface modifications by functional groups [40] (e.g. $–NH_2$, $–SO_3H$, and –C–OH, etc) are also effective in improving the reaction kinetics. It is worthy to notice that the affection of some oxygen-containing groups, however, reduces the kinetics of V^{3+}/V^{2+} and VO_2^+/VO^{2+} [41].

Precipitation inhibitors can be used to stabilize VO_2^+ ions in sulfuric acid and thus increase the concentration [42, 43]. Skyllas-Kazacos *et al* [43] investigated the effects of phosphate additives, including ammonium phosphate ($(NH_4)_3PO_4$), potassium phosphate (K_3PO_4), sodium hexametaphosphate ($Na_6[(PO_3)_6]$), phosphoric acid (H_3PO_4), as well as the ammonium sulfates ($(NH_4)_2SO_4$). The H_3PO_4 (1 wt.%) and $(NH_4)_2SO_4$ (2 wt.%) combination prevent V^{5+} precipitating at a high temperature of 45 °C thanks to the molecular interactions between VO_2^+ cations and NH_4^+/PO_4^{3-} ions. More than that, $(NH_4)_2SO_4$ can enhance the stability of V^{3+} in sulfuric acid at a low temperature of 5 °C, offering a wide operating temperature range [44]. Other additives, such as polyacrylic acid [45] and trishydroxymethyl aminomethane [46, 47], also show proven efficacy in stabilizing the vanadium electrolytes.

Recent studies also focus on the fabrication of electrodes [48], application of novel membranes [49, 50], and the design of battery configurations. For instance, the modification of bipolar plates and flow field can effectively improve the overall performance [51, 52].

2.2.1.2. Fe-based redox couples. The low redox potential of the plating and stripping of Fe render the Fe^{2+}/Fe couple available as the anode reaction:

$$Fe^{2+} + e^- \leftrightarrow Fe \quad E^0 = -0.44 \text{ V vs SHE.}$$

Apparently, the redox potential is 440 mV lower than for HER, suggesting that HER could cause coulombic losses during the plating and stripping of Fe [53]. Upon HER, pH may rise locally at the electrode surface or even in the bulk electrolyte, causing the precipitation of iron complexes. Buffering agents, ascorbic acid and citric acid for instance, prevent the rapid pH changes during the plating and stripping of iron [54, 55]. HER can be inhibited by increasing the electrolyte pH or limiting the mass transport of hydronium ions (H_3O^+). Increasing the pH of the electrolyte will shift the equilibrium potential for HER more negatively and slow down the mass transport. For example, Savinell *et al* [56] reported that the HER current decreased from 15 to 0.7 mA cm^{-2} at −0.8 V (vs Ag/AgCl) as the pH value increased from 1 to 3. However, if the pH increases beyond 3, Fe^{2+} will precipitate as hydroxides. Another approach to suppress HER is to remove potential absorption sites for protons by electrolyte additives, Cl^- for instance (figure 4(A)) [56]. Depositing a thin metal layer (e.g. In, Cd) with a high overpotential of HER can also inhibit HER [55].

The Fe^{3+}/Fe^{2+} couple is an excellent catholyte component:

$$Fe^{3+} + e^- \leftrightarrow Fe^{2+} \quad E^0 = 0.77 \text{ V vs SHE.}$$

The redox potential is pH-independent and has the standard rate constant (k^0) of 1.2×10^{-4} cm s^{-1} [57]. Fe^{3+} ions are stable in a strong acidic solution but will hydrolyze and form $Fe(OH)_3$ precipitations even at a low concentration of 10^{-6} M when the pH value exceeds 2 at 25 °C [58]. One approach to prevent this issue is to link $Fe^{3+/2+}$ ions with ligands. Ferricyanide ($[Fe(CN)_6]^{3-}$) and ferrocyanide ($[Fe(CN)_6]^{4-}$) are stable in a pH range extending to mild alkaline regime conditions due to the strong coordination of cyanide ions to the iron

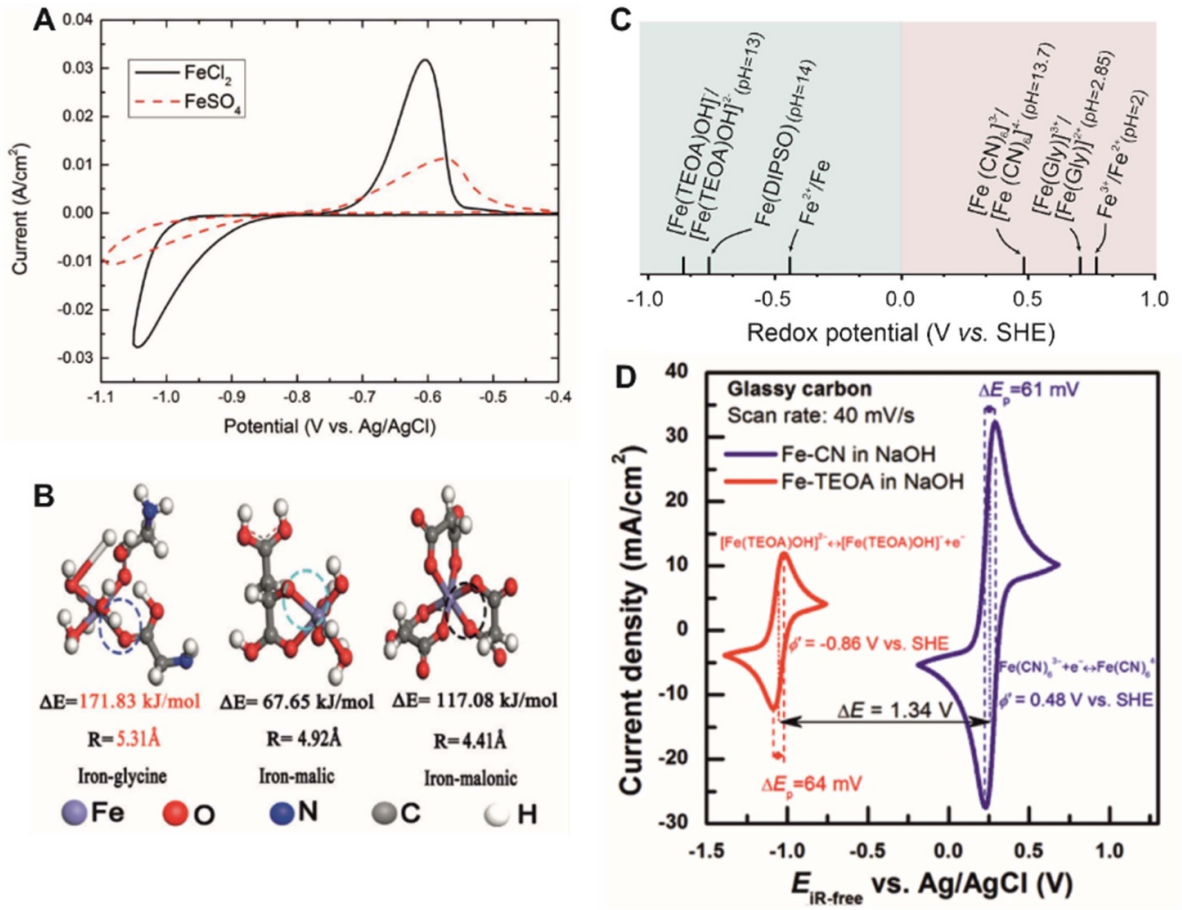

Figure 4. Iron-based redox couples. (A) CV curves of iron plating/stripping in chloride and sulfate electrolytes. The adsorption of Cl^- onto the electrode alleviates HER and enhances the iron plating/stripping kinetics. Reproduced with permission [56]. Copyright © 2014 The Electrochemical Society. Reproduced by permission of IOP Publishing Ltd. (B) Binding energies and radius of iron complexes with glycine, malic and malonic. Reproduced with permission [24]. Copyright 2017, John Wiley & Sons. (C) Redox potentials of water-soluble iron complexes. TEOA: triethanolamine; Gly: glycine; DIPSO: 3-[bis (2-hydroxyethyl) amino]-2-hydroxypropanesulfonic acid. (D) CV curves of $[Fe(TEOA)OH]^-/[Fe(TEOA)OH]^{2-}$ and $Fe(CN)_6^{3-}/Fe(CN)_6^{4-}$ in sodium hydroxide solution. Reproduced with permission [23]. Copyright 2016, American Chemical Society.

center. The standard potential of $[Fe(CN)_6]^{3-}/[Fe(CN)_6]^{4-}$ reaction is 0.36 V vs SHE. As $[Fe(CN)_6]^{3-}$ will decompose in a strong alkaline electrolyte, a neutral electrolyte shows improved stability for the $[Fe(CN)_6]^{3-}/[Fe(CN)_6]^{4-}$ redox couples [59]. Besides, cations for $[Fe(CN)_6]^{3-}$ and $[Fe(CN)_6]^{4-}$ play an important role in the cell energy density because they would increase the solubility of $[Fe(CN)_6]^{3-}$ and $[Fe(CN)_6]^{4-}$. For example, the solubility of $(NH_4)_4[Fe(CN)_6]$ is 1.6 M in the water while it is only 0.56 M for $Na_4[Fe(CN)_6]$ [60].

Ligands alleviate ion crossover due to the large size of the complexes. A large ligand, such as glycine, offers a large complex with a radius of 5.31 Å (figure 4(B)), suppressing the hydrolysis of Fe^{3+}/Fe^{2+} due to the high binding energy and reducing the crossover rate [24]. Chelation of ligands reduces the activation energy of electron transfer of Fe^{3+}/Fe^{2+}, thus improving the reaction kinetics [61–64]. Moreover, the variation of the electron cloud of iron by complexing with different ligands leads to a range of reduction potentials (figure 4(C)), providing diverse matchups for the iron-based redox electrolytes. For instance, a couple of $[Fe(CN)_6]^{3-}/[Fe(CN)_6]^{4-}$ as catholyte and $[Fe(TEOA)OH]^-/[Fe(TEOA)OH]^{2-}$ (−0.86 V vs SHE) as anolyte shows a voltage of 1.34 V in an alkaline electrolyte (figure 4(D)) [23].

2.2.1.3. Cr^{3+}/Cr^{2+} redox couples. The first aqueous redox flow battery was invented and launched by NASA in the 1970s, in which the Fe^{3+}/Fe^{2+} couple as the catholyte and the Cr^{3+}/Cr^{2+} pair as the anolyte. The redox reaction of Cr^{3+}/Cr^{2+} is expressed by the following equation [65]:

$$Cr^{3+} + e^- \leftrightarrow Cr^{2+} \quad E^0 = -0.41 \text{ V vs SHE.}$$

As the redox potential is more than 400 mV lower than that for HER, such a redox reaction often exhibits a low coulombic efficiency due to the parasitic HER process. Additionally, the sluggish kinetics of Cr^{3+}/Cr^{2+} is relatively low, which requires the incorporation of catalysts to facilitate the redox reaction [66].

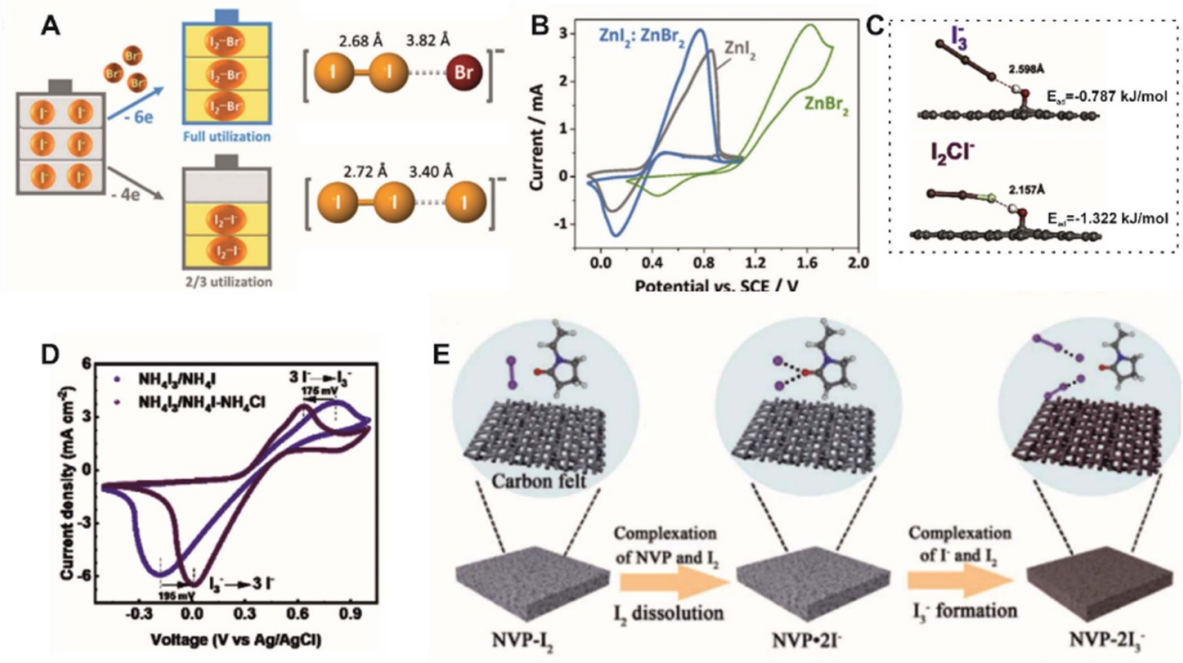

Figure 5. Iodide-based redox couples. (A) Conceptual illustration of bromide as the complexing agent to stabilize iodine and the corresponding structure of I_2Br^- and I_3^- ions. Both ions have a linear (or nearly linear) structure and are thermodynamically stable. (B) CV curves of ZnI_2, $ZnBr_2$ and the mixed electrolytes. Reproduced with permission [72]. Copyright 2017, Royal Society of Chemistry. (C) Density functional theory (DFT)-optimized molecular structure of the I_3^-, and I_2Cl^- anions at the surface of OH-functionalized graphite cathode. (D) CV curves of NH_4I_3/NH_4I with or without NH_4Cl. Reproduced with permission [73]. Copyright 2020, Elsevier. (E) Illustration of polyiodide-NVP complex formation. Reproduced with permission [75]. Copyright 2021, Royal Society of Chemistry.

2.2.1.4. Halogen-based redox couples. Iodide (I^-) shows high solubility in aqueous and non-aqueous media. The oxidation of iodide to iodine (I_2) is followed by the formation of triiodide (I_3^-) through I^- complexation [67, 68]:

$$2I^- - 2e^- \leftrightarrow I_{2(aq)} \quad E^0 = 0.621 \text{ V vs SHE}$$

$$I_2 + I^- \rightarrow I_3^-.$$

Accordingly, excessive iodide ions are used as a complexing agent to stabilize the free iodine, thus giving an overall reaction as follows [69, 70]:

$$3I^- - 2e^- \leftrightarrow I_3^- \quad E^0 = 0.536 \text{ V vs SHE}.$$

The I_3^-/I^- couple, instead of the redox couple of I_2/I^-, is used in catholyte [71]. However, the low utilization of I^- limits its volumetric capacity and therefore energy density. Complexed with other halogen elements, such as bromide ions, more I^- ions were involved in the energy storage because I_2 can be stabilized by complexing with bromide ions (I_2Br^-, figure 5(A)) [72]. Meanwhile, the generation of corrosive bromine was excluded during redox reactions (figure 5(B)). As a result, a high energy density of 202 Wh l^{-1} based on the catholyte volume was achieved in a Zn/iodine-bromine (I_2Br^-) flow battery. Iodine-chloride (I_2Cl^-) was also capable of increasing the cell capacity [73]. I_2Cl^- anions not only improves the reaction reversibility (figure 5(C)), but also shows high adsorption energy to the OH-functionalized graphite felt as evidenced by the reducing X–H bond length (figure 5(D)). In practice, I_3^- can be oxidized to solid-state I_2 by overcharging, and the accumulated I_2 forms a film on the electrode, blocking the pore of electrodes and the pumps or pipelines [74]. Carbonyl groups in N-vinylpyrrolidone (NVP) can break I–I bonds in I_2, forming NVP-$2I_3^-$ (figure 5(E)) [75]. Therefore, NVP is an excellent additive to prevent the accumulation of I_2.

Despite all these downsides brought by solid I_2, the liquid-solid conversion of I^- to I_2 can realize an almost 100% utilization of I^-, offering a high energy density of 205 Wh l^{-1} approaching its theoretical energy density [76]. In this case, the pump and pipeline blockage caused by solid I_2 can be bypassed by avoiding electrolyte circulation.

Likewise, many bromide salts are highly soluble in water. A high redox potential of the Br_2/Br^- couple (1.08 V vs SHE) contributes to a high cell voltage. Similar to iodide oxidation, bromine molecules can combine with bromide ions to generate tribromide ions [77]:

$$2Br^- - 2e^- \leftrightarrow Br_2 \quad E^0 = 1.08 \text{ V vs SHE}$$

$$Br_2 + Br^- \rightarrow Br_3^-.$$

As a result, the overall reaction is:

$$3Br^- - 2e^- \leftrightarrow Br_3^-.$$

Several redox couples have been employed to pair with Br_2/Br^- cathode to generate aqueous redox flow batteries, such as zinc-bromine, vanadium-bromine, hydrogen-bromine and quinone-bromine cells. However, the high toxicity (0.1 ppm of OSHA Permissible Exposure Limit) and high vapor pressure (28.8 kPa at 25 °C) should be considered in practical use. Complexing with a ligand is also an effective method to mitigate the toxicity of Br_2.

2.2.1.5. Polysulfide-based redox couples. Sulfur and polysulfides show rich and complicated chemistry. Transformation of polysulfides with different chain lengths show solid–liquid, liquid–liquid, and even the solid–solid conversion. Such diverse reactions offer broad opportunities to design high-capacity batteries. Unlike in an organic solvent, in which long-chain polysulfides (e.g. Li_2Sn, $n \geqslant 4$) can be dissolved, short-chain polysulfides (including Li_2Sn, Na_2Sn, and K_2Sn, $1 \leqslant n \leqslant 4$) are highly soluble in water. The negative redox potential of the transition between various polysulfides enables their application of anolyte in flow batteries [78, 79]:

$$S_4^{2-} + 2e^- \leftrightarrow 2S_2^{2-} \quad E^0 = -0.51\,\text{V vs SHE}$$

$$S_2^{2-} + 2e^- \leftrightarrow 2S^{2-} \quad E^0 = -0.51\,\text{V vs SHE.}$$

The former reaction has a lower capacity of 418 mAh g^{-1} while the latter offers a superior capacity of 837 mAh g^{-1}. In addition, a shorter chain shows improved kinetics. The rate of mass transport is lower than the charge transfer process without strong convection (e.g. stirring). Therefore, external stirring or circulation of electrolyte and the regulation of electrolyte concentration have been frequently used to enhance the mass transport to alleviate the concentration polarization. Plenty of approaches have been employed to boost the performance of S-based aqueous batteries. A detailed review on polysulfide redox couples has recently been given by Chao *et al* [80].

2.2.2. Liquid–solid redox couples

2.2.2.1. MnO_2(s)/Mn^{2+} redox couple. Manganese (Mn) has diverse valence states (i.e. 0, +2, +3, +4, +6 and +7) offering rich redox chemistry. The charge storage of Mn-based cathodes often relies on solid-state conversion and cation (Na^+, Zn^{2+} and H^+) intercalation. The mass-loading of active electrode materials predetermines the capacity. Recently, the deposition-dissolution reaction of the MnO_2/Mn^{2+} redox couple was proposed by Cui *et al* in a MnO_2-H_2 battery [81]. $MnSO_4$ was oxidized to MnO_2 on conductive materials (e.g. carbon felt and graphite) following the chemical reaction:

$$Mn^{2+} + 2H_2O \rightarrow MnO_2 + 4H^+ + 2e^-$$
$$E^0 = 1.23\ \text{V vs SHE.}$$

The two-electron transfer allows for a high theoretical capacity of about 616 mAh g^{-1} based on the mass of MnO_2. Two mechanisms were proposed: (a) hydrolysis in neutral electrolyte and (b) disproportionation in acidic electrolyte. Both mechanisms start with the oxidation of Mn^{2+} forming Mn^{3+} through a one-electron reaction. Subsequently, Mn^{3+} are hydrolyzed and precipitate as MnOOH on the surface electrode, which is further oxidized to MnO_2 in a neutral solution or undergoes a disproportionation reaction producing soluble Mn^{2+} and Mn^{4+} ions hydrolyzed to MnO_2 in an acidic solution. As Mn^{3+} is stable in the acidic solution, the mixed oxidation state of Mn^{3+} and Mn^{4+} are often found in the electrodeposited manganese oxide. Qiao *et al* [82] compared the electrodeposited MnO_2 from a solution (1 M $ZnSO_4$ and 1 M $MnSO_4$) with and without adding 0.1 M H_2SO_4. The mixed oxidation state of Mn^{4+}/Mn^{3+} in the electrodeposited MnO_x was derived from x-ray photoelectron spectra and Mn-$L_{2,3}$ electron energy loss spectra (EELS) (figure 6(A)). Mn vacancies were directly observed in the MnO_2 obtained from the mildly acidic solution (figure 6(B)). The increased surface energy density from Mn vacancies reduces the energy barrier and accelerates the dissolution of MnO_2 (figures 6(C) and (D)).

However, the disproportionation reaction of Mn^{3+} species reduces the energy density because fewer electrons can be stored (figure 5(E)). Moreover, the accumulation of stable Mn^{3+} species causes a capacity decrease over cycling. To alleviate these issues, Li *et al* [83] conceived the idea to oxidize Mn^{2+} to MnO_2 by coordinating with acetate ions (Ac^-):

$$2MnAc_2 + 2H_2O - 2e^- \rightarrow MnO_2 + 4HAc + Mn^{2+}.$$

In this case, $Mn(Ac)_2$ is added to the electrolyte. The reaction exhibits high reversibility. The oxidation potential of MnO_2 in the $Mn(Ac)_2$ system is 0.53 V, lower than in $MnSO_4$ (figure 5(F)), which is ascribed to the lower Gibbs free energy of HAc that requires less energy to trigger the oxidization.

2.2.2.2. Zn-based redox couples. Zinc (Zn) metals have advantages of low cost, high capacity, and inherent stabilities in air and aqueous solutions. The plating-stripping process of Zn features different couples with a variation in pH. The detailed reactions in different media are as follows:

$$Zn^{2+} + 2e^- \leftrightarrow Zn \quad E^0 = -0.76\,\text{V vs SHE}$$

$$Zn(OH)_4^{2-} + 2e^- \leftrightarrow Zn + 4OH^- \quad E^0 = -1.22\,\text{V vs SHE.}$$

The redox potential of Zn/Zn^{2+} is −0.76 V (vs SHE) in neutral or mild acidic electrolytes. However, Zn metal suffers from severe dendrite growth and accompanied HER process. In alkaline electrolytes, the $Zn(OH)_4{}^{2-}$/Zn couple exhibits fast kinetics and a much lower redox potential [84]. Nevertheless, the Zn reversibility still decreases due to the formation of byproducts.

2.2.2.3. Sn-based redox couples. Tin (Sn) can be reversibly stripped and plated at a potential of −0.13 V (vs SHE):

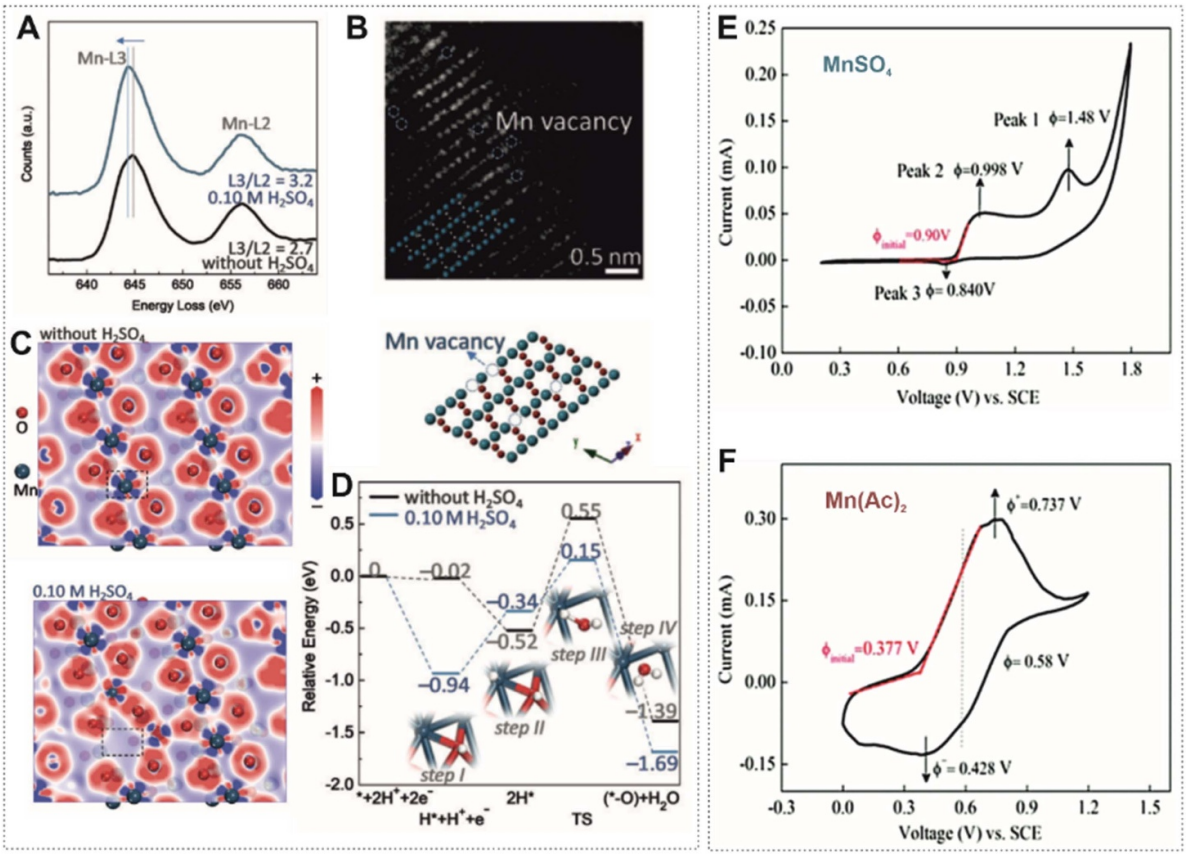

Figure 6. Oxidation of Mn^{2+}. (A) Mn-$L_{2,3}$ EELS of the electrodeposited MnO_2 from the electrolyte with and without H_2SO_4. The left-shift of the Mn-L_3 peak of MnO_2 and the increased L_3/L_2 value indicate the variation in the valence state of Mn. (B) Atomic-resolution high-angle annular dark-field scanning transmission electron microscopy image and crystal structure with exposed (101) facets and Mn vacancies (dotted circles). (C) Electron density difference of vacancy-free MnO_2 (without H_2SO_4, top) and MnO_2 with vacancies (0.10 M H_2SO_4, bottom). (D) Relative energy profiles along the reaction pathway (steps I–IV). Insets are schematics of the electrolytic reaction pathways. Reproduced with permission [82]. Copyright 2019, John Wiley & Sons. CV curves of (E) 0.05 M $MnSO_4$ in 0.5 M K_2SO_4 and (F) 0.05 M $Mn(Ac)_2$ in 1 M KCl at a scan rate of 10 mV s^{-1}. Reproduced with permission [83]. Copyright 2020, Royal Society of Chemistry.

$$Sn^{2+} + 2e^- \leftrightarrow Sn \quad E^0 = -0.13 \text{ V vs SHE.}$$

The high diffusivity of Sn^{2+} ions in chloride acid (1.67×10^{-5} cm^2 s^{-1}) and fast reaction kinetic constant (2.02×10^{-4} cm s^{-1}) guarantee good performance as a redox-active electrolyte [22]. Moreover, in an alkaline electrolyte, the $Sn(OH)_6^{2-}$/Sn electrode shows a smooth and dendrite-free morphology due to the intrinsic low-surface-energy anisotropy that facilitates the isotropic crystal growth of the Sn metal. As a result, the $Sn(OH)_6^{2-}$/Sn anolyte offers high reversibility of up to 500 stable cycles (more than two months) [85].

2.3. *Water-soluble organic electrolytes*

Organic redox-active species often have tunable potentials by designing functional groups. For instance, the reduction potential of quinones decreases because electron-donating groups (e.g. –OH and $–NH_2$) increase molecular orbital energies. On the contrary, electron-withdrawing substituents (e.g. $–SO_3H$) reduce the molecular orbital energies, thus raising the reduction potential [86–89]. The pH variation also influences the redox potential of quinone-based redox couples. The tunable redox potential allows for the design of all quinone-based battery system [87, 90]. Similar phenomenon can be found on 2,2,6,6-tetramethylpiperidine-1-oxyl (TEMPO) derivatives. Redox-active nitroxyl radicals show tunable potentials with various functional groups [91]. However, TEMPO derivatives are generally employed in the catholyte due to their relatively positive potential [92].

The functional groups also play an important role in manipulating the solubility of organic redox species. For instance, methyl viologen (4,4′-dimethyl bipyridinium dichloride, MVi^{2+}) has a high solubility of 3 M in water. It undergoes a two single-electron reduction at negative potentials (−0.45 V and −0.76 V vs SHE). The first reduction shows high reversibility, while the second one becomes quasi-reversible due to the low solubility of the corresponding reduction product, which is a common dilemma for viologen-based redox couples. Many efforts have been carried out on enhancing the solubility of the final reduction product by substituting with a hydrophilic functional group (e.g. hydrophilic ammonium or sulfonate functional group) to enable high reversibility of the second reduction [87, 90, 93–95]. In addition, Viologens and TEMPO derivatives show high stability

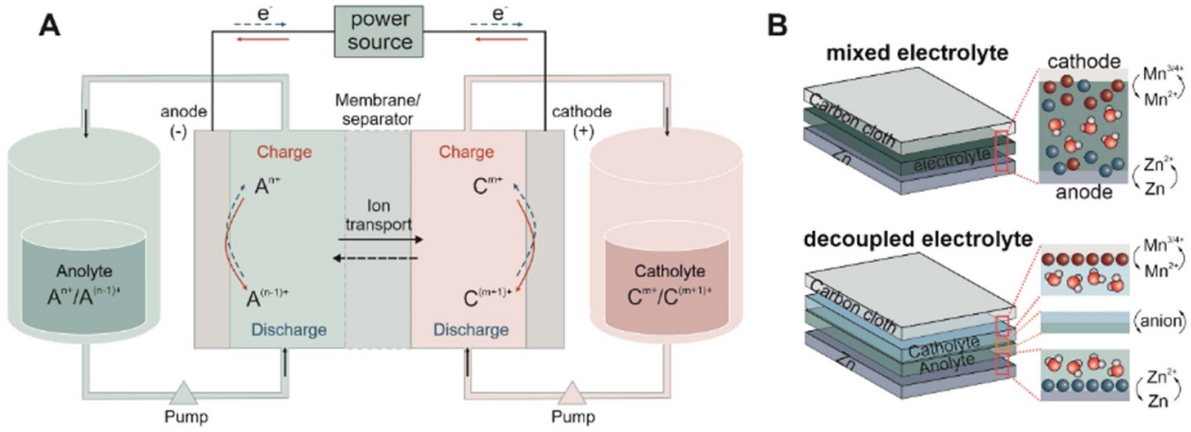

Figure 7. From large-scale to portable devices. Schematic illustration of (A) a conventional redox-flow battery for large scale storage (Reproduced with permission [2]. Copyright 2016, Springer Nature) and (B) a simple sandwich-structured MnO_2–Zn battery with mixed (upper panel) and decoupled hydrogel electrolyte (bottom panel) for portable devices. Reproduced with permission [98]. Copyright 2021, American Chemical Society.

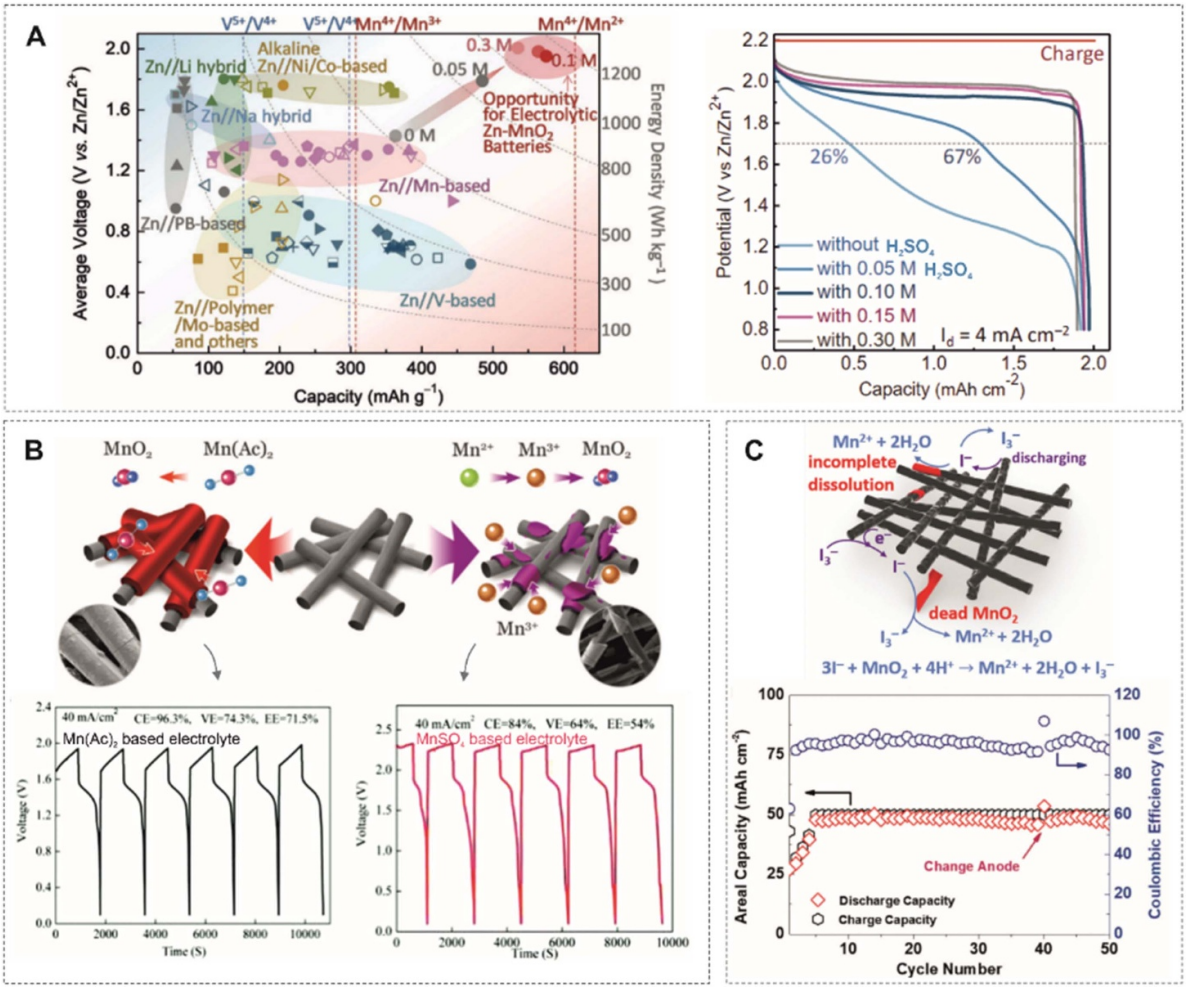

Figure 8. MnO_2/Mn^{2+} deposition/dissolution chemistry. (A) Performance comparison of electrolytic Zn–MnO_2 battery among state-of-the-art Zn metal batteries and galvanostatic discharge curves of electrolytic Zn–MnO_2 battery in acidic electrolyte. Reproduced with permission [82]. Copyright 2019, John Wiley & Sons. (B) Direct two-electron transfer of the Mn^{2+}/MnO_2 couple by changing the electrolyte with acetate radicals and the corresponding charge/discharge curves of Zn–MnO_2 batteries in $Mn(Ac)_2$ and $MnSO_4$ based electrolytes. Reproduced with permission [83]. Copyright 2020, Royal Society of Chemistry. (C) Conceptual illustration of KI as a mediator and cycling stability of Zn–MnO_2 battery with 0.1 M KI at a high charge capacity of 50 mAh cm^{-2} at 20 mA cm^{-2}. Reproduced with permission [99]. Copyright 2021, Royal Society of Chemistry.

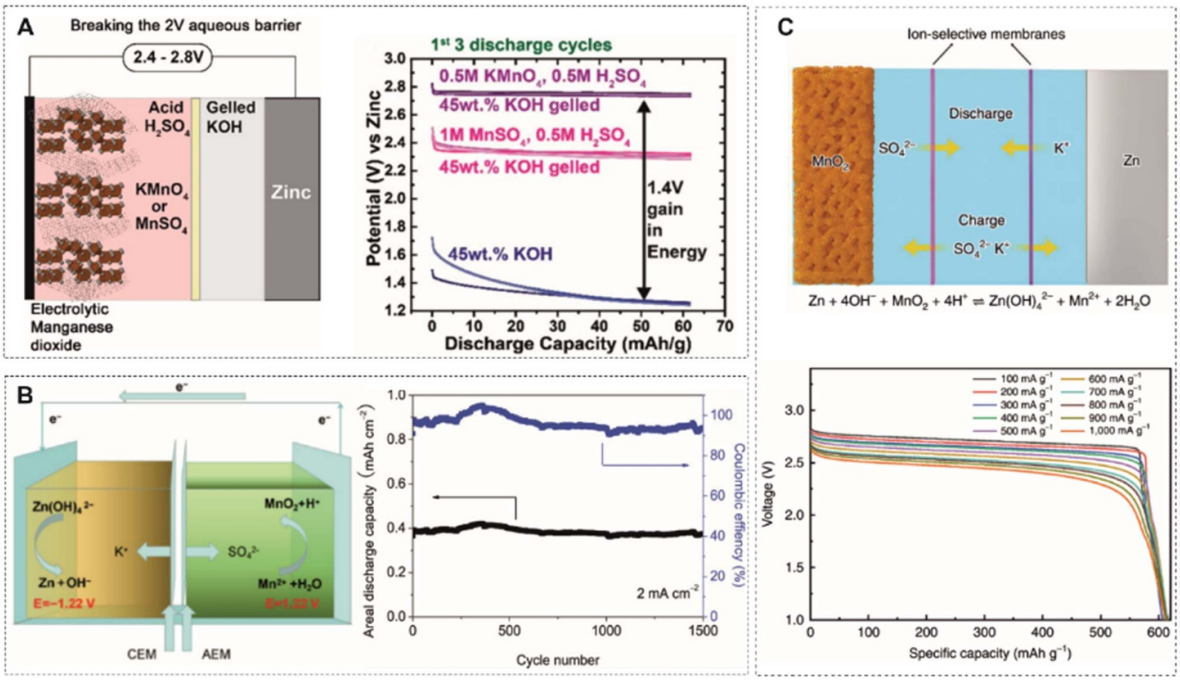

Figure 9. MnO_2/Mn^{2+} deposition/dissolution chemistry with decoupled electrolytes. (A) Illustration of Zn–MnO_2 batteries with an acidic catholyte and an alkaline gelated anolyte and discharge curves with and without decoupled electrolytes. Reproduced with permission [101]. Copyright 2019, American Chemical Society. (B) Schematic illustration and mechanism of electrolytic Zn–MnO_2 battery in decoupled electrolytes separated by a bipolar membrane (at charge state) and the cycle performance of the Zn–MnO_2 stationary battery. Reproduced with permission [102]. Copyright 2020, John Wiley & Sons. (C) Schematic diagram and discharge curves at different current densities of the battery with decoupled reactions in acidic catholyte and alkaline anolyte separated by an ion-selective membrane. Reproduced with permission [103]. Copyright 2020, Springer Nature.

in the neutral electrolytes and therefore a broad potential window [96, 97].

3. From large-scale storage to portable devices

Redox-flow batteries storing the redox-active electrolytes in external tanks (figure 7(A)) represent a straightforward design to unleash the energy storage ability of electrolytes. Catholytes and anolytes are stored in independent reservoirs and circulated with an exterior pump. The continuous supply of electrolytes via circulation can reduce the concentration polarization by refilling redox-active species timely after they are consumed to store energy. Carbon-based materials (e.g. carbon felts or carbon papers) are widely used as electrodes because they provide abundant active sites for redox reactions. Further modification on the carbon surface and electrocatalysts are used to improve energy efficiency. A membrane, known as an ion-selective membrane, is placed between the catholyte and anolyte to prevent the ion crossover.

A simplified design was created by using an electrolyte containing redox-active species for cathodic and anodic reactions. For instance, the $ZnBr_2$ electrolyte offers Zn^{2+}/Zn and Br^-/Br redox couples. The ion transportation of anions should be fast enough to warrant redox reactions at the cathode without the external circulation force. A zinc-iodine (Zn-I) single flow battery shows a high energy density of 205 Wh l^{-1} (theoretical energy density is about 240 Wh l^{-1} based on the electrolyte volume). The combination of a highly ionic conductive polyolefin separator and highly cation-selective Nafion thin membrane results in high energy efficiency.

When used in portable devices, it is impossible to circulate the redox-active electrolytes from an external electrolyte tank. As a result, cell structures follow the conventional design with a sandwich structure (figure 7(B)). Mn^{2+}/Mn^{4+} and Zn/Zn^{2+} redox couples were first investigated to unleash the energy storage in the electrolyte because they share the same device structure as alkaline or neutral Zn–MnO_2 batteries. Qiao *et al* [82] applied MnO_2/Mn^{2+} conversion in an acidic electrolyte (figure 8(A)). The battery exhibits a high discharge voltage (∼1.95 V). With a high capacity of 571 mAh g^{-1}, the battery delivers a high energy density of 409 Wh kg^{-1} based on the total mass of active materials. Despite the fast kinetics of MnO_2/Mn^{2+} conversion, the side reaction of Mn^{3+} disproportionation would inhibit the conversion efficiency between MnO_2 and Mn^{2+}. In general, the oxidation states of Mn^{3+} and Mn^{4+} are observed in the deposited MnO_2. To improve the energy efficiency, Li *et al* replaced $MnSO_4$ by $Mn(Ac)_2$ (figure 8(B)), which enables the direct conversion from Mn^{2+} to MnO_2 by coordinating Ac^- anions [83]. Although the battery exhibits a lower discharge voltage plateau (∼1.5 V) than for the $MnSO_4$ electrolyte (∼1.8 V), higher efficiencies, including coulombic efficiency, voltage and energy efficiency, were achieved. The battery worked well with an area capacity of 20 mAh cm^{-2}, which was previously limited to 10 Ma h cm^{-2}. Lu *et al* introduced an iodide

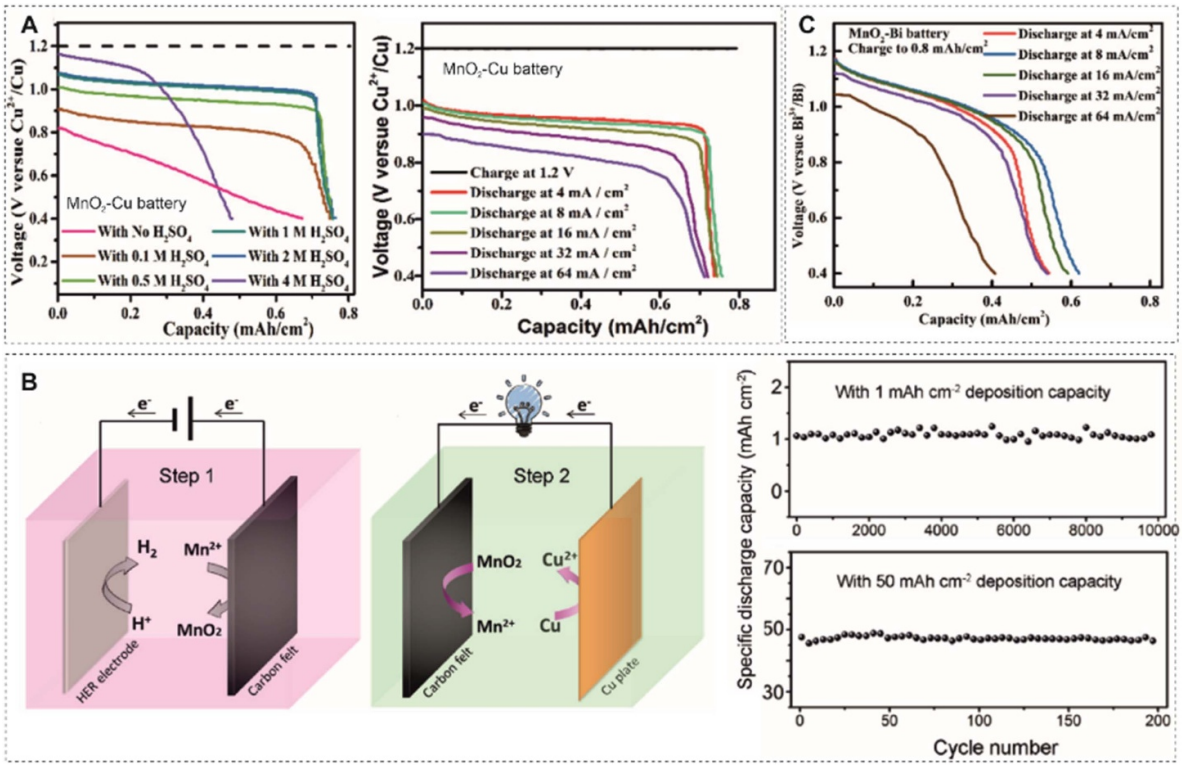

Figure 10. MnO_2/Mn^{2+} deposition/dissolution chemistry coupled with Cu and Bi. (A) Discharge curves of MnO_2–Cu battery with different acid concentrations when charged to 0.8 mAg cm^{-2} and at different current densities with 0.5 M H_2SO_4. Reproduced with permission [105]. Copyright 2019, John Wiley & Sons. (B) Demonstration of the combination system between MnO_2–Cu cell and hydrogen evolution and the electrochemical performance of the MnO_2–Cu cell. Reproduced with permission [106]. Copyright 2019, Elsevier. (C) Discharge curves of MnO_2–Bi battery at different current densities when charged to 0.8 mAh cm^{-2}. Reproduced with permission [105]. Copyright 2019, John Wiley & Sons.

(I_3^-) redox mediator into the electrolyte to reduce the 'dead' and undissolved MnO_2 (figure 8(C)), increasing the charge capacity up to 50 mAh cm^{-2} [99]. Likewise, Chen *et al* [100] employed Br_3^-/Br^- mediator to improve the dissolution of the over deposited MnO_2 and enhance the reversibility of the cathodic reaction. The acidic electrolyte facilitates the Mn^{2+}/Mn^{4+} conversion but brings a high risk of Zn corrosion. Zhu *et al* [98] decoupled the electrolyte into acidic catholyte and mild anolyte in the gel state, resulting in more than two times higher capacity and rate capability.

Based on the decoupled design, the anolyte can be changed to an alkaline solution to further reduce the redox potential of the anode. The $Zn(OH)_4^{2-}/Zn$ redox couple in the alkaline media has a potential of −1.22 V vs SHE, which is about 0.46 V lower than for mild and acidic electrolytes. Banerjee *et al* [101] came up with a design based on an acidic-alkaline dual electrolyte, which exhibits a 2.45 V open circuit voltage. The MnO_2 pre-coated carbon felt is immersed in an acidic liquid electrolyte, and the Zn anode is surrounded by a polymerized gelled alkaline electrolyte (figure 9(A)). The decoupled electrolyte removes the limit of water splitting at 1.23 V and therefore expands the electrochemical stability window of the electrolyte. Liu *et al* [102] presented a similar design by using the liquid acid-alkaline electrolyte. The catholyte contains 1 M $MnSO_4$ and 0.5 M H_2SO_4, and the anolyte consists of 0.1 M $Zn(Ac)_2$ and 2.4 M KOH (figure 9(B)). To prevent neutralization, two solutions are separated by a bipolar membrane, anion exchange membrane and cation exchange membrane. The battery shows a high CE of 98.4% and cycling stability of 97.5% retention over 1500 cycles. As the potential of MnO_2/Mn^{2+} conversion is pH-dependent, the cell voltage can be further raised to 2.65 V by employing a strong acidic catholyte with 3 M H_2SO_4 (figure 9(C)) [103]. In particular, the battery has a discharge plateau as high as ∼2.71 V at a current density of 100 mA g^{-1} with a specific capacity of 616 mAh g^{-1}, achieving ∼100% of the theoretical capacity of the two-electron transfer process of Mn^{4+}/Mn^{2+}. Both high working voltage and specific capacity enable a high energy density of 1621.7 Wh kg^{-1} based on the mass of MnO_2. Moreover, the battery shows a superior cycling stability of 200 h (116 deep cycles) due to the enhanced dissolution of MnO_2 during discharge in strong acid. The adsorbed hydrogen ions on the MnO_2 surface facilitate the formation of oxygen vacancies and lead to Mn atoms being exposed on the surface. It is also possible to introduce a catalyst, such as Ni, to catalyze MnO_2/Mn^{2+} conversion [104].

Other metal-based anodes (e.g. Cu, Bi, Pb) are also paired with MnO_2/Mn^{2+}. For instance, MnO_2–Cu and MnO_2–Bi batteries were proposed by Zhi *et al* [105]. The MnO_2–Cu battery exhibits an average discharge plateau at ∼0.95 V in an acidic electrolyte (figure 10(A)). It shows a stable rate capability with only a 6.6% decrement as the discharge current

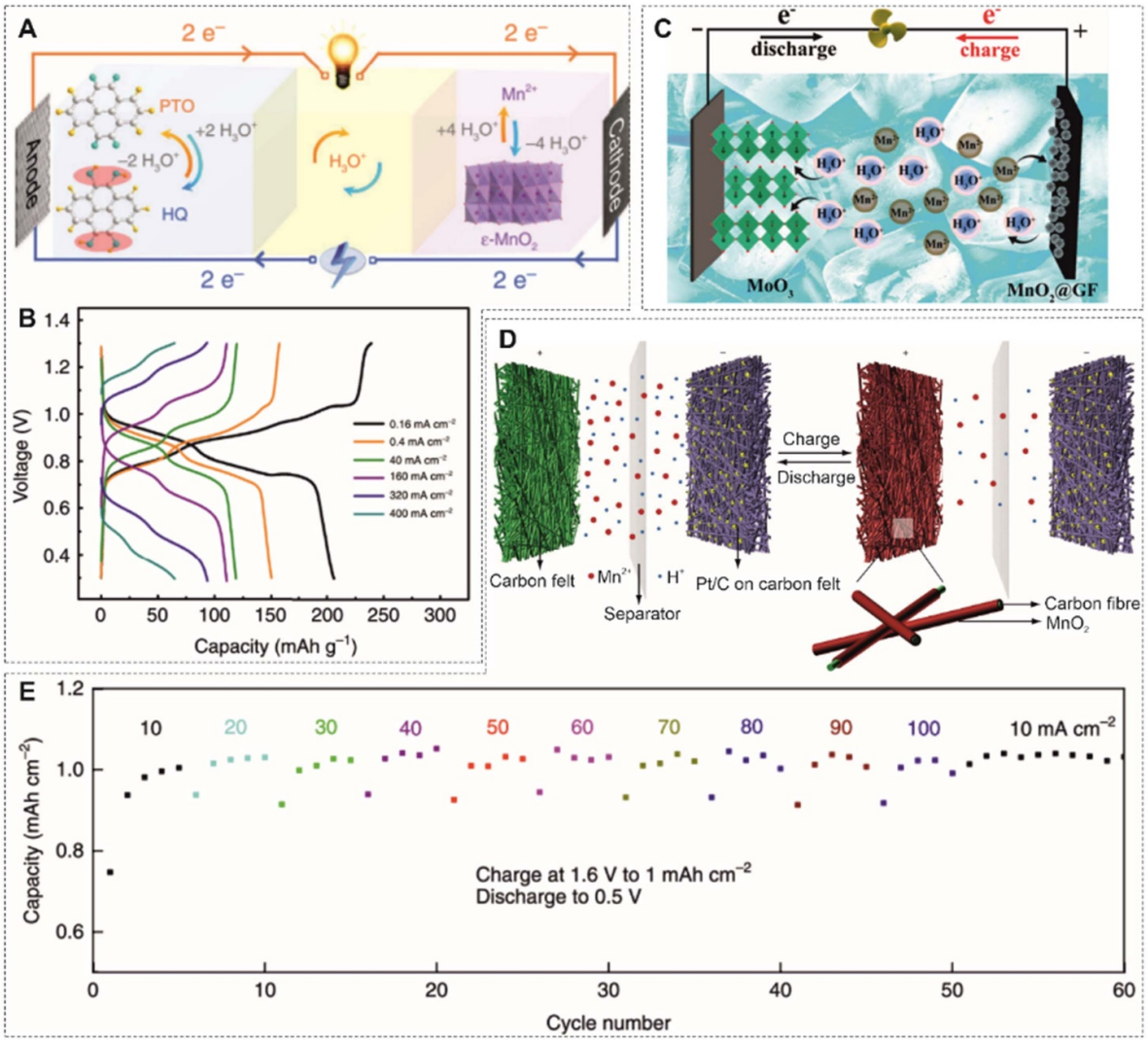

Figure 11. MnO_2/Mn^{2+} deposition/dissolution chemistry with proton anodes. (A) Schematic illustration and working mechanism for the PTO-MnO_2@GF hydronium-ion battery. (B) Galvanostatic charge/discharge curves of PTO-electrode at different current densities. Reproduced with permission [107]. Copyright 2020, Springer Nature, CC BY 4.0. (C) Schematic illustration of MnO_3-MnO_2@GF proton battery. Reproduced with permission [108]. Copyright 2020, American Chemical Society. (D) Mn–H battery in the charge and discharge modes. (E) Rate capability in electrolyte of 1 M $MnSO_4$ with 0.05 M H_2. Reproduced with permission [81]. Copyright 2018, Springer Nature.

density increases from 4 to 64 mA cm^{-2} and a lifetime of 2000 cycles under a charge capacity of 0.8 mAh cm^{-2} at 16 mA cm^{-2}. During long-term cycling the coulombic efficiency range fluctuates between 123.8% and 84.8%, which might be associated with the insertion of ions (H^+ and Cu^{2+}) into undissolved MnO_2. Xia *et al* [106] prolonged the lifetime of a MnO_2–Cu battery to 10 000 cycles under 1 mAh cm^{-2} capacity at 10 mA cm^{-2} without capacity decay. It used a high concentration of $MnSO_4$ and $CuSO_4$, up to 0.8 M. The cell capacity can reach up to 50 mAh cm^{-2} with a coulombic efficiency of 96% and a high energy efficiency beyond 70% (figure 10(B)). The energy density attains 40.8 Wh l^{-1}. The MnO_2–Bi battery displays a stable rate capability (∼0.4 mAh cm^{-2} at 64 mA cm^{-2} when charged to 0.8 mAh cm^{-2}) in an acidic electrolyte but with a coulombic efficiency lower than 80% due to the uncomplete dissolution of MnO_2 and the quasi-reversible plating and stripping process of the Bi metal (figure 10(C)) [105].

Besides metallic anodes, proton-coupled redox pairs can also be used as active species for the anode. Wang *et al* proposed a hydronium-ion battery, where pyrene-4,5,9,10-tetraone (PTO) was used as the anode [107]. The formed hydronium ions (H_3O^+) shuttle between electrodes, initiating a quinone/hydroquinone redox reaction at the anode and MnO_2/Mn^{2+} conversion reaction at the cathode. A high power density of 30.8 kW kg^{-1} based on the total mass of PTO and deposited MnO_2 is attainable due to the good diffusivity of hydronium ions (figures 11(A) and (B)). Moreover, the electrolyte still shows a high conductivity in a frozen state, enabling the operation of the battery from −40 °C to −70 °C. MoO_3 also hosts H_3O^+ ions, which exhibits a power density of 66.6 kW kg^{-1} (figure 11(C)) [108]. Hydrogen can be

directly used as the anode. Cui *et al* [81] proposed a Mn–H battery, where a Pt/C coated carbon felt was employed as the catalyst and conductive materials for H_2 evolution. The 1 M MnSO4 electrolyte was optimized by adding 0.05 M H_2SO_4. The Mn–H battery exhibits a discharge voltage of ∼1.3 V, a good capacity of nearly 1 mAh cm^{-2}, reaching almost 100% coulombic efficiency at 100 mA cm^{-2} (36 s of discharge), and a lifetime of more than 10 000 cycles without capacity decay (figures 11(D) and (E)).

4. Conclusions and outlook

The energy storage capacity of the electrolyte has shown its promise to further increase the energy density of batteries. However, such designs are mainly employed at the grid-scale and are rarely used in portable or microdevices. In order to fabricate excellent portable aqueous batteries based on such designs, both the working mechanisms and the technical construction are indispensable.

First of all, the working mechanisms are instructive roles to design energy storage devices with high electrochemical performance. However, the working mechanisms of the aforementioned redox-active electrolytes in the non-flow designs are still not fully uncovered. For example, protons are important for the reversibility of the Mn^{2+}/MnO_2 couple. Nevertheless, Mn^{3+} disproportionation reactions often occur with a high proton concentration, impairing the coulombic efficiency. A Zn-rich composite layer was found on the surface of MnO_2 during the charging process, but it disappeared by discharging [109]. However, the exact crystal structure and function in energy storage process are still unknown. Thus, *in-situ* investigations, especially those focusing on the interface, would be helpful to reveal the reactions of the redox-active species in the electrolyte. Without a precise working mechanism, it is hard to develop effective ways to simultaneously improve the reversibility and efficiency of charge storage.

In addition to the working mechanism, the compatibility of materials with device fabrication procedures is also critical. Carbon felt has been frequently used as the current collector due to its high electrical conductivity. The porous structure provides abundant electrochemically active sites and reduces the areal current density, and the 3D matrix can accommodate high mass loading of MnO_2 thus approaching a high charge capacity. However, if shrink the scale of the battery to a millimeter or even a micrometer, the carbon felt would be not available. The graphene or metal materials through physical vapor deposition or other deposition techniques should be considered. The deposited membranes are generally not able to offer such a 3D matrix unless with a design of 3D structures. It would also be a good approach to fabricate a planar thin film with a large footprint to introduce more redox reaction sites and shrink the footprint to form a Swiss-roll configuration through rolled-up nanotechnology. In addition, the accumulation and dissolution of redox products that introduce repeated and significant stress variation also impose a challenge in the mechanical stability of current collectors, especially for microscale devices that contain a thin current collector. The selection of the counter electrode is essential to the overall electrochemical performance. For instance, the dendrite formation and HER are two challenges using Zn as the anode. The optimized electrolyte for independent half-cells is not always applicable for a full cell. The addition of protons in the MnO_2/Mn^{2+} deposition/dissolution system increases the reversibility; however, the high acidity accelerates the corrosion of Zn anode.

Besides, exploring a suitable solid-state electrolyte is an essential step toward practical use. Unlike common solid-state electrolytes that focus primarily on ionic conductivity, redox-active solid-state electrolytes also need to guarantee the redox activity of the ions. More importantly, the solid-solid interface between the electrolyte and electrode (current collector) after accumulating redox products needs to maintain the reactivity. The selection of packaging materials with high stability is often overlooked but important for the lifetime of actual devices.

Apart from the mechanism and battery fabrication, the operation protocols need to be different with different chemistry. The charging process determines the capacity of the battery using the redox-active electrolyte. With the increase in charge capacity, the current collector will be coated with a thicker material layer. The poor electrical conductivity of deposits would impair the reversibility. Accumulation of inactive deposits will eventually delaminate from the current collector, causing unwanted effects, such as short-cuts. Therefore, each electrolyte with redox activity should have its own optimal charging and discharging procedure and target specific application scenarios. It is a promising energy storage system by triggering and unleashing the energy storage ability of active species in electrolytes and it still needs more effort to put in, facilitating its development from grid-scale to a portable application or even a millimeter/micrometer scale.

Acknowledgments

M Zhu acknowledges the support by the German Research Foundation DFG (ZH 989/2-1). O G Schmidt acknowledges financial support by the Leibniz Program of the German Research Foundation (SCHM 1298/26-1). H Tang, Z Qu, W Zhang and H Zhang acknowledge the support and funding from China Scholarship Council (CSC).

ORCID iD

Minshen Zhu https://orcid.org/0000-0001-5883-4962

References

[1] Gür T M 2018 Review of electrical energy storage technologies, materials and systems: challenges and prospects for large-scale grid storage *Energy Environ. Sci.* **11** 2696–767

[2] Park M, Ryu J, Wang W and Cho J 2017 Material design and engineering of next-generation flow-battery technologies *Nat. Rev. Mater.* **2** 16080

[3] Faisal M *et al* 2018 Review of energy storage system technologies in microgrid applications: issues and challenges *IEEE Access* **6** 35143–64

[4] Pal B, Yang S, Ramesh S, Thangadurai V and Jose R 2019 Electrolyte selection for supercapacitive devices: a critical review *Nanoscale Adv.* **1** 3807–35

[5] Lee J *et al* 2019 Redox-electrolytes for non-flow electrochemical energy storage: a critical review and best practice *Prog. Mater. Sci.* **101** 46–89

[6] Borenstein A *et al* 2017 Carbon-based composite materials for supercapacitor electrodes: a review *J. Mater. Chem.* A **5** 12653–72

[7] Simon P and Gogotsi Y 2020 Perspectives for electrochemical capacitors and related devices *Nat. Mater.* **19** 1151–63

[8] Choi C *et al* 2020 Achieving high energy density and high power density with pseudocapacitive materials *Nat. Rev. Mater.* **5** 5–19

[9] Kumar K S, Choudhary N, Jung Y and Thomas J 2018 Recent advances in two-dimensional nanomaterials for supercapacitor electrode applications *ACS Energy Lett.* **3** 482–95

[10] Leung P *et al* 2012 Progress in redox flow batteries, remaining challenges and their applications in energy storage *RSC Adv.* **2** 10125–56

[11] Zhang J *et al* 2018 An all-aqueous redox flow battery with unprecedented energy density *Energy Environ. Sci.* **11** 2010–5

[12] Liu Z *et al* 2020 Voltage issue of aqueous rechargeable metal-ion batteries *Chem. Soc. Rev.* **49** 180–232

[13] Chao D and Qiao S Z 2020 Toward high-voltage aqueous batteries: super- or low-concentrated electrolyte? *Joule* **4** 1846–51

[14] Yang Z *et al* 2011 Electrochemical energy storage for green grid *Chem. Rev.* **111** 3577–613

[15] Ulaganathan M *et al* 2016 Recent advancements in all-vanadium redox flow batteries *Adv. Mater. Interfaces* **3** 1500309

[16] Wu M C, Zhao T S, Wei L, Jiang H R and Zhang R H 2018 Improved electrolyte for zinc-bromine flow batteries *J. Power Sources* **384** 232–9

[17] Kolthoff I M and Tomsicek W J 1935 The oxidation potential of the system potassium ferrocyanide-potassium ferricyanide at various ionic strengths *J. Phys. Chem.* **4** 945–54

[18] Quan M, Sanchez D, Wasylkiw M F and Smith D K 2007 Voltammetry of quinones in unbuffered aqueous solution: reassessing the roles of proton transfer and hydrogen bonding in the aqueous electrochemistry of quinones *J. Am. Chem. Soc.* **129** 12847–56

[19] Delahay P, Pourbaix M and Van Rysselberghe P 1951 Potential-pH diagram of zinc and its applications to the study of zinc corrosion *J. Electrochem. Soc.* **98** 101

[20] Beh E S *et al* 2017 A neutral pH aqueous organic–organometallic redox flow battery with extremely high capacity retention *ACS Energy Lett.* **2** 639–44

[21] Bard A J and Faulkner L R 2000 *Electrochemical Methods: Fundamentals and Applications* (New York: Wiley)

[22] Zhou X, Lin L, Lv Y, Zhang X and Wu Q 2018 A Sn-Fe flow battery with excellent rate and cycle performance *J. Power Sources* **404** 89–95

[23] Gong K *et al* 2016 All-soluble all-iron aqueous redox-flow battery *ACS Energy Lett.* **1** 89–93

[24] Xie C, Duan Y, Xu W, Zhang H and Li X 2017 A low-cost neutral zinc–iron flow battery with high energy density for stationary energy storage *Angew. Chem., Int. Ed.* **56** 14953–7

[25] Nicholson R S 1965 Theory and application of cyclic voltammetry for measurement of electrode reaction kinetics *Anal. Chem.* **37** 1351–5

[26] Hofmann J D and Schröder D 2019 Which parameter is governing for aqueous redox flow batteries with organic active material? *Chem. Ing. Tech.* **91** 786–94

[27] Michibata H 2012 *Vanadium: Biochemical and Molecular Biological Approaches. Vanadium: Biochemical and Molecular Biological Approaches* (Dordrecht: Springer) pp 228

[28] Vijayakumar M, Wang W, Nie Z, Sprenkle V and Hu J 2013 Elucidating the higher stability of vanadium(V) cations in mixed acid based redox flow battery electrolytes *J. Power Sources* **241** 173–7

[29] Li L *et al* 2011 A stable vanadium redox-flow battery with high energy density for large-scale energy storage *Adv. Energy Mater.* **1** 394–400

[30] Agarwal H, Florian J, Goldsmith B R and Singh N 2019 V^{2+}/V^{3+} redox kinetics on glassy carbon in acidic electrolytes for vanadium redox flow batteries *ACS Energy Lett.* **4** 2368–77

[31] Suárez D J *et al* 2014 Graphite felt modified with bismuth nanoparticles as negative electrode in a vanadium redox flow battery *ChemSusChem* **7** 914–8

[32] Jiang H R *et al* 2020 A high power density and long cycle life vanadium redox flow battery *Energy Storage Mater.* **24** 529–40

[33] Tseng T-M, Huang R-H, Huang C-Y, Hsueh K-L, Shieu F-S and Kinetic A 2013 Study of the platinum/carbon anode catalyst for vanadium redox flow battery *J. Electrochem. Soc.* **160** A690–6

[34] Tsai H M, Yang S J, Ma C C M and Xie X 2012 Preparation and electrochemical activities of iridium-decorated graphene as the electrode for all-vanadium redox flow batteries *Electrochim. Acta* **77** 232–6

[35] Kim K J *et al* 2012 Novel catalytic effects of Mn_3O_4 for all vanadium redox flow batteries *Chem. Commun.* **48** 5455–7

[36] Ejigu A, Edwards M and Walsh D A 2015 Synergistic catalyst-support interactions in a graphene-Mn_3O_4 electrocatalyst for vanadium redox flow batteries *ACS Catal.* **5** 7122–30

[37] Thu Pham H T, Jo C, Lee J and Kwon Y 2016 MoO_2 nanocrystals interconnected on mesocellular carbon foam as a powerful catalyst for vanadium redox flow battery *RSC Adv.* **6** 17574–82

[38] Zhou H *et al* 2014 CeO_2 decorated graphite felt as a high-performance electrode for vanadium redox flow batteries *RSC Adv.* **4** 61912–8

[39] Shen Y *et al* 2014 Electrochemical catalytic activity of tungsten trioxide-modified graphite felt toward VO_2^+/VO^{2+} redox reaction *Electrochim. Acta* **132** 37–41

[40] Shah A B, Wu Y and Joo Y L 2019 Direct addition of sulfur and nitrogen functional groups to graphite felt electrodes for improving all-vanadium redox flow battery performance *Electrochim. Acta* **297** 905–15

[41] Li Y, Parrondo J, Sankarasubramanian S and Ramani V 2019 Impact of surface carbonyl- and hydroxyl-group concentrations on electrode kinetics in an all-vanadium redox flow battery *J. Phys. Chem.* C **123** 6370–8

[42] Roe S, Menictas C and Skyllas-Kazacos M 2016 A high energy density vanadium redox flow battery with 3 M vanadium electrolyte *J. Electrochem. Soc.* **163** A5023–8

[43] Kausar N, Mousa A and Skyllas-Kazacos M 2016 The effect of additives on the high-temperature stability of the vanadium redox flow battery positive electrolytes *ChemElectroChem* **3** 276–82

[44] Mousa A and Skyllas-Kazacos M 2015 Effect of additives on the low-temperature stability of vanadium redox flow

battery negative half-cell electrolyte *ChemElectroChem* **2** 1742–51
[45] Zhang J *et al* 2011 Effects of additives on the stability of electrolytes for all-vanadium redox flow batteries *J. Appl. Electrochem.* **41** 1215–21
[46] Peng S *et al* 2012 Influence of trishydroxymethyl aminomethane as a positive electrolyte additive on performance of vanadium redox flow battery *Int. J. Electrochem. Sci.* **7** 2440-47
[47] Peng S *et al* 2012 Stability of positive electrolyte containing trishydroxymethyl aminomethane additive for vanadium redox flow battery *Int. J. Electrochem. Sci.* **7** 4388–96
[48] Li Q, Bai A, Xue Z, Zheng Y and Sun H 2020 Nitrogen and sulfur co-doped graphene composite electrode with high electrocatalytic activity for vanadium redox flow battery application *Electrochim. Acta* **362** 137223
[49] Bhushan M, Kumar S, Singh A K and Shahi V K 2019 High-performance membrane for vanadium redox flow batteries: cross-linked poly(ether ether ketone) grafted with sulfonic acid groups via the spacer *J. Membr. Sci.* **583** 1–8
[50] Si J, Lv Y, Lu S and Xiang Y 2019 Microscopic phase-segregated quaternary ammonia polysulfone membrane for vanadium redox flow batteries *J. Power Sources* **428** 88–92
[51] Yin C, Gao Y, Xie G, Li T and Tang H 2019 Three dimensional multi-physical modeling study of interdigitated flow field in porous electrode for vanadium redox flow battery *J. Power Sources* **438** 227023
[52] Tsushima S and Suzuki T 2020 Modeling and simulation of vanadium redox flow battery with interdigitated flow field for optimizing electrode architecture *J. Electrochem. Soc.* **167** 020553
[53] Zeng Y K, Zhao T S, Zhou X L, Wei L and Ren Y X 2017 A novel iron-lead redox flow battery for large-scale energy storage *J. Power Sources* **346** 97–102
[54] Manohar A K *et al* 2016 A high efficiency iron-chloride redox flow battery for large-scale energy storage *J. Electrochem. Soc.* **163** A5118–25
[55] Jayathilake B S, Plichta E J, Hendrickson M A and Narayanan S R 2018 Improvements to the coulombic efficiency of the iron electrode for an all-iron redox-flow battery *J. Electrochem. Soc.* **165** A1630–8
[56] Hawthorne K L, Petek T J, Miller M A, Wainright J S and Savinell R F 2015 An investigation into factors affecting the iron plating reaction for an all-iron flow battery *J. Electrochem. Soc.* **162** A108–13
[57] Holze R and Lechner M D 2007 *Electrochemistry : Electrochemical Thermodynamics and Kinetics* (Berlin: Springer)
[58] Beverskog B 1996 Revised diagrams for iron at 25–300 °C *Corros. Sci.* **38** 2121–35
[59] Luo J *et al* 2017 Unraveling pH dependent cycling stability of ferricyanide/ferrocyanide in redox flow batteries *Nano Energy* **42** 215–21
[60] Luo J *et al* 2019 Unprecedented capacity and stability of ammonium ferrocyanide catholyte in pH neutral aqueous redox flow batteries *Joule* **3** 149–63
[61] Yee E L, Cave R J, Guyer K L, Tyma P D and Weaver M J 1979 A survey of ligand effects upon the reaction entropies of some transition metal redox couples *J. Am. Chem. Soc.* **101** 1131–7
[62] Chen Y D, Santhanam K S V and Bard A J 1981 Solution redox couples for electrochemical energy storage: I. Iron (III)-iron (II) complexes with O-phenanthroline and related ligands *J. Electrochem. Soc.* **128** 1460–7
[63] Weber A Z *et al* 2011 Redox flow batteries: a review *J. Appl. Electrochem.* **41** 1137–64
[64] Waters S E, Robb B H, Marshak M P and Marshak M P 2020 Effect of chelation on iron-chromium redox flow batteries *ACS Energy Lett.* **5** 1758–62
[65] Lopez-Atalaya M, Codina G, Perez J R, Vazquez J L and Aldaz A 1992 Optimization studies on a Fe/Cr redox flow battery *J. Power Sources* **39** 147–54
[66] Wang W *et al* 2013 Recent progress in redox flow battery research and development *Adv. Funct. Mater.* **23** 970–86
[67] Gwynne E, Davies B H and Gwynne E 1952 The iodine-iodide interaction *J. Am. Chem. Soc.* **I** 2748–52
[68] McIndoe J S and Tuck D G 2003 Studies of polyhalide ions in aqueous and non-aqueous solution by electrospray mass spectrometry *Dalton Trans.* **2003** 244–8
[69] Zhao Y, Wang L and Byon H R 2013 High-performance rechargeable lithium-iodine batteries using triiodide/iodide redox couples in an aqueous cathode *Nat. Commun.* **4** 1–7
[70] Li B *et al* 2015 Ambipolar zinc-polyiodide electrolyte for a high-energy density aqueous redox flow battery *Nat. Commun.* **6** 6303
[71] Li Z, Weng G, Zou Q, Cong G and Lu Y C 2016 A high-energy and low-cost polysulfide/iodide redox flow battery *Nano Energy* **30** 283–92
[72] Weng G M, Li Z, Cong G, Zhou Y and Lu Y C 2017 Unlocking the capacity of iodide for high-energy-density zinc/polyiodide and lithium/polyiodide redox flow batteries *Energy Environ. Sci.* **10** 735–41
[73] Mousavi M *et al* 2020 Decoupled low-cost ammonium-based electrolyte design for highly stable zinc–iodine redox flow batteries *Energy Storage Mater.* **32** 465–76
[74] Jang W J, Cha J S, Kim H and Yang J H 2021 Effect of an iodine film on charge-transfer resistance during the electro-oxidation of iodide in redox flow batteries *ACS Appl. Mater. Interfaces* **13** 6385–93
[75] Yang J, Song Y, Liu Q and Tang A 2021 High-capacity zinc-iodine flow batteries enabled by a polymer-polyiodide complex cathode *J. Mater. Chem.* A **9** 16093–8
[76] Xie C, Liu Y, Lu W, Zhang H and Li X 2019 Highly stable zinc-iodine single flow batteries with super high energy density for stationary energy storage *Energy Environ. Sci.* **12** 1834–9
[77] Luo J *et al* 2019 A 1.51 v pH neutral redox flow battery towards scalable energy storage *J. Mater. Chem.* A **7** 9130–6
[78] Zhang S *et al* 2019 Recent progress in polysulfide redox-flow batteries *Batter. Supercaps* **2** 627–37
[79] Gross M M and Manthiram A 2019 Long-life polysulfide-polyhalide batteries with a mediator-ion solid electrolyte *ACS Appl. Energy Mater.* **2** 3445–51
[80] Liu J *et al* 2021 Sulfur-based aqueous batteries: electrochemistry and strategies *J. Am. Chem. Soc.* **143** 15475–89
[81] Chen W *et al* 2018 A manganese-hydrogen battery with potential for grid-scale energy storage *Nat. Energy* **3** 428–35
[82] Chao D *et al* 2019 An electrolytic Zn–MnO_2 battery for high-voltage and scalable energy storage *Angew. Chem., Int. Ed.* **58** 7823–8
[83] Xie C *et al* 2020 A highly reversible neutral zinc/manganese battery for stationary energy storage *Energy Environ. Sci.* **13** 135–43
[84] Gong K *et al* 2015 A zinc-iron redox-flow battery under $100 per kW h of system capital cost *Energy Environ. Sci.* **8** 2941–5
[85] Yao Y, Wang Z, Li Z and Lu Y-C 2021 A dendrite–free tin anode for high-energy aqueous redox flow batteries *Adv. Mater.* **33** 2008095

[86] Huskinson B *et al* 2014 A metal-free organic-inorganic aqueous flow battery *Nature* **505** 195–8

[87] Yang B, Hoober-Burkhardt L, Wang F, Surya Prakash G K and Narayanan S R 2014 An inexpensive aqueous flow battery for large-scale electrical energy storage based on water-soluble organic redox couples *J. Electrochem. Soc.* **161** A1371–80

[88] Er S, Suh C, Marshak M P and Aspuru-Guzik A 2015 Computational design of molecules for an all-quinone redox flow battery *Chem. Sci.* **6** 885–93

[89] Wedege K, Dražević E, Konya D and Bentien A 2016 Organic redox species in aqueous flow batteries: redox potentials, chemical stability and solubility *Sci. Rep.* **6** 1–13

[90] Yang B *et al* 2016 High-performance aqueous organic flow battery with quinone-based redox couples at both electrodes *J. Electrochem. Soc.* **163** A1442–9

[91] Zhou W *et al* 2020 Fundamental properties of TEMPO-based catholytes for aqueous redox flow batteries: effects of substituent groups and electrolytes on electrochemical properties, solubilities and battery performance *RSC Adv.* **10** 21839–44

[92] Nutting J E, Rafiee M and Stahl S S 2018 Tetramethylpiperidine N-oxyl (TEMPO), phthalimide N-oxyl (PINO), and related N-oxyl species: electrochemical properties and their use in electrocatalytic reactions *Chem. Rev.* **118** 4834–85

[93] DeBruler C *et al* 2017 Designer two-electron storage viologen anolyte materials for neutral aqueous organic redox flow batteries *Chemistry* **3** 961–78

[94] Jin S *et al* 2020 Near neutral pH redox flow battery with low permeability and long-lifetime phosphonated viologen active species *Adv. Energy Mater.* **10** 2000100

[95] Liu W *et al* 2019 A highly stable neutral viologen/bromine aqueous flow battery with high energy and power density *Chem. Commun.* **55** 4801–4

[96] Liu T, Wei X, Nie Z, Sprenkle V and Wang W 2016 A total organic aqueous redox flow battery employing a low cost and sustainable methyl viologen anolyte and 4-HO-TEMPO catholyte *Adv. Energy Mater.* **6** 1501449

[97] Janoschka T *et al* 2015 An aqueous, polymer-based redox-flow battery using non-corrosive, safe, and low-cost materials *Nature* **527** 78–81

[98] Tang H *et al* 2021 Battery-everywhere design based on a cathodeless configuration with high sustainability and energy density *ACS Energy Lett.* **6** 1859–68

[99] Lei J, Yao Y, Wang Z and Lu Y C 2021 Towards high-areal-capacity aqueous zinc-manganese batteries: promoting MnO_2 dissolution by redox mediators *Energy Environ. Sci.* **14** 4418–26

[100] Zheng X *et al* 2021 Boosting electrolytic MnO_2-Zn batteries by a bromine mediator *Nano Lett.* **21** 8863–71

[101] Yadav G G, Turney D, Huang J, Wei X and Banerjee S 2019 Breaking the 2 V barrier in aqueous zinc chemistry: creating 2.45 and 2.8 V MnO_2-Zn aqueous batteries *ACS Energy Lett.* **4** 2144–6

[102] Liu C, Chi X, Han Q and Liu Y 2020 A high energy density aqueous battery achieved by dual dissolution/deposition reactions separated in acid-alkaline electrolyte *Adv. Energy Mater.* **10** 1903589

[103] Zhong C *et al* 2020 Decoupling electrolytes towards stable and high-energy rechargeable aqueous zinc–manganese dioxide batteries *Nat. Energy* **5** 440–9

[104] Chao D *et al* 2020 Atomic engineering catalyzed MnO_2 electrolysis kinetics for a hybrid aqueous battery with high power and energy density *Adv. Mater.* **32** 2001894

[105] Liang G *et al* 2019 A universal principle to design reversible aqueous batteries based on deposition–dissolution mechanism *Adv. Energy Mater.* **9** 1901838

[106] Huang J *et al* 2019 Low-cost and high safe manganese-based aqueous battery for grid energy storage and conversion *Sci. Bull.* **64** 1780–7

[107] Guo Z *et al* 2020 An organic/inorganic electrode-based hydronium-ion battery *Nat. Commun.* **11** 959

[108] Yan L *et al* 2020 Solid-state proton battery operated at ultralow temperature *ACS Energy Lett.* **55** 685–91

[109] Wu T H, Lin Y Q, Althouse Z D and Liu N 2021 Dissolution-redeposition mechanism of the MnO_2 cathode in aqueous zinc-ion batteries *ACS Appl. Energy Mater.* **4** 12267–74